ACS OMEGA

http://pubs.acs.org/journal/acsodf

Article

Millimeter-Scale $Zn(3\text{-ptz})_2$ Metal−Organic Framework Single Crystals: Self-Assembly Mechanism and Growth Kinetics

Juan M. Garcia-Garfido, Javier Enríquez, Ignacio Chi-Durán, Iván Jara, Leonardo Vivas, Federico J. Hernández, Felipe Herrera,* and Dinesh P. Singh*

Cite This: https://doi.org/10.1021/acsomega.1c01272

Read Online

ACCESS | Metrics & More | Article Recommendations | Supporting Information

ABSTRACT: The solvothermal synthesis of metal−organic frameworks (MOFs) often proceeds through competing crystallization pathways, and only partial control over the crystal nucleation and growth rates is possible. It challenges the use of MOFs as functional devices in free-space optics, where bulk single crystals of millimeter dimensions and high optical quality are needed. We develop a synthetic protocol to control the solvothermal growth of the MOF $[Zn(3\text{-ptz})_2]_n$ (MIRO-101), to obtain large single crystals with projected surface areas of up to 25 mm^2 in 24 h, in a single reaction with in situ ligand formation. No additional cooling and growth steps are necessary. We propose a viable reaction mechanism for the formation of MIRO-101 crystals under acidic conditions, by isolating intermediate crystal structures that directly connect with the target MOF and reversibly interconverting between them. We also study the nucleation and growth kinetics of MIRO-101 using ex situ crystal image analysis. The synthesis parameters that control the size and morphology of our target MOF crystal are discussed. Our work deepens our understanding of MOF growth processes in solution and demonstrates the possibility of building MOF-based devices for future applications in optics.

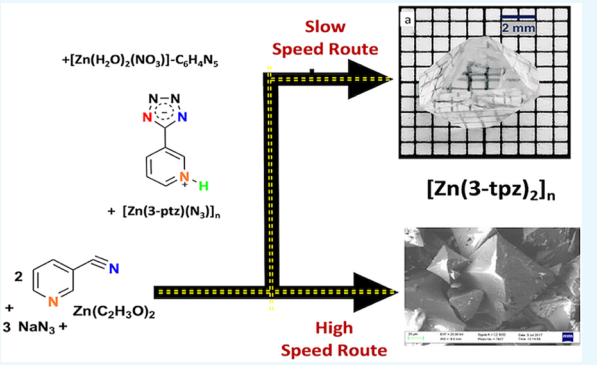

INTRODUCTION

Metal−organic frameworks (MOFs) are an established class of porous materials with demonstrated use in a wide range of applications that benefit from their record-high surface areas, including gas storage,[1] gas separation,[1,2] water purification,[3] fuel cells,[4] drug delivery,[5,6] catalysis,[7] and chemical sensing.[8,9] MOFs are also considered as promising materials for applications in nonlinear optics,[10−14] given the variety of noncentrosymmetric structures with large optical nonlinearities that can be formed,[11,12] in comparison with the limited number of inorganic standards available in the industry.

Contrary to MOF applications that rely on crystal pore engineering, MOF crystals with small porosities are most favorable in optics. Large pore sizes reduce the thermal conductivity of the material and can result in the loss of crystallinity through moisture adsorption.[15] Both effects are detrimental to the performance of an optical crystal under normal laser operation.[16] In addition to the constraints on the chemical composition and unit cell symmetry, which determine the intrinsic optical quality (e.g., transparency and birefringence), future applications of MOFs in optics demand strict constraints on the crystal size and morphology.[17] For nonlinear optics, large transparent crystals with propagation lengths and transverse areas in the millimeter range are needed to achieve conditions of energy and momentum conservation (phase matching), between the optical waves that mix in a nonlinear process.[18] Although frequency doubling with MOFs has been demonstrated for several polycrystalline samples,[11] phase matching in the powder form is imperfect, and the generated nonlinear output lacks the temporal coherence properties needed for future optical applications.[17] This is the case of the noncentrosymmetric MOF $[Zn(3\text{-ptz})_2]_n$ that displays a moderate powder second-harmonic generation (SHG) response (ca. 0.4 times than that of urea),[19] enabling its applicability as a nonlinear optics material. Nevertheless, SHG information is limited because phase matching conditions cannot be satisfied in the powder form.[11] Hence, high-quality single crystals of millimeter dimensions instead of crystalline powder samples are required to achieve more accurate and reliable optical characterization.[11,20] Although efforts have been dedicated to study the factors that control the self-assembly and crystallization processes of MOF structures,[21] a general understanding of growth processes is still elusive, which limits the strategies for the growth of large-sized single crystals of MOFs for nonlinear optics application.

Received: March 9, 2021
Accepted: May 14, 2021

It is known that the size and morphology of MOF crystals depend on synthesis parameters such as molar ratio, solvent polarity, reaction temperature, pH, and additives.[22] Additives can control the concentration of crystal precursors (e.g., ligands), which effectively modulates the crystal growth kinetics. Commonly used modulators include polymers,[23] surfactants,[24,25] organic salts,[26−28] organic oil,[29] and organic and inorganic acids.[30−34] Millimeter-sized MOF-5[32] and $Cu_3(BTC)_2$[33] centrosymmetric single crystals ($Fm3m$ space group) have been recently achieved using acid modulators, for applications in liquid phase chromatography. These large-sized single crystals were obtained using a standard slow evaporation method at 85 °C for several days. The proposed modulation mechanism involved the suppressed deprotonation of the ligand (HBTC), with the subsequently reduced availability of the coordinating species (BTC^-) in solution.

In this work, we demonstrate the controlled growth and tunable morphology of MOF $[Zn(3\text{-ptz})_2]_n$ (MIRO-101) single crystals under solvothermal conditions using suitable acid modulators. This MOF was first obtained in a powder form by Wang et al.[19] through an in situ ligand formation reaction using the Demko−Sharpless method.[35] Building on our previous results,[36−39] we carry out the first mechanistic study of the solvothermal self-assembly process of MIRO-101 crystals, by considering a range of temperatures, pHs, and ionic strengths. We identify and isolate a set of MOF crystals and other metal complexes that are directly involved in the formation mechanism of the target MOF and then reversibly interconvert between them. Given the large crystal size and yields obtained, we are able to quantify the nucleation and growth rates of MIRO-101 via ex situ crystal image processing and discuss the results in terms of plausible kinetic models. Our work thus deepens our understanding of MOF formation processes in solution and represents an enabling step in the application of MIRO-101 crystals for future applications in free-space optics.[40]

RESULTS AND DISCUSSION

We synthesize MOF $[Zn(3\text{-ptz})_2]_n$ (MIRO-101) crystals following the previous methodology,[36,37] by adjusting the reaction mixture pH from 2.54 to 5.35 using nitric acid, as described in Experimental Section. The mixture is brought to 105 °C in a standard box furnace (for details, see Experimental Section), for a reaction time varying from 90 min to 40 h. Product MIRO-101 crystals of various sizes were collected at high temperature (>80 °C), and their crystalline purity was confirmed by powder XRD. The filtered solution was allowed to cool to room temperature (RT), from where colorless crystals were isolated for further characterization.

In Figure 1a, we show a single crystal sample obtained at pH 2.7, for a reaction time of 24 h and a molar ratio of 2:4:6 (acetate zinc/3-cyanopyridine/sodium azide). Single crystals with linear dimensions of about 6−8 mm can be reproducible by carefully controlling the reaction temperature and dilution level (further details are given in Experimental Section). The large crystal sizes achieved allow for standard polishing techniques, which we use to prepare transparent MOF slabs with transverse dimensions in the range of 0.2−0.3 mm (Figure 1b) and cross-sectional areas in the range of 2−6 mm (Figure 1c,d). As we discuss in what follows, the crystal size distribution is strongly dependent on the pH, temperature, and reaction time.

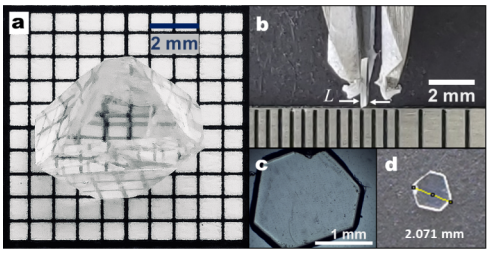

Figure 1. Large-sized $Zn(3\text{-ptz})_2$ MOF single crystal. (a) As-synthesized raw crystal sample with octahedron habit. (b) Polished crystal slab with a transverse propagation length L = 0.22 mm. (c) Optical image of the polished slab showing point-like surface opacities. (d) Image with linear dimensions of the transverse area.

We study the size distribution of the as-synthesized MIRO-101 crystals on the reaction pH and time, at a fixed reaction temperature (105 °C). Immediately after the reaction is completed, the MOF crystals formed are filtered while hot and brought to RT. The entire crystal sample is photographed over a scaled background with a digital camera (ex situ imaging). The image is processed, as detailed in Experimental Section, to obtain a histogram of the crystal areas projected on the image plane. In Figure 2a, we show the preprocessed image of an MOF crystal sample synthesized at pH 4.0 in 24 h. The corresponding area histogram is shown in Figure 2b. In general, the MOF samples obtained have individual single crystals of various sizes and also relatively large polycrystals are formed by the agglomeration of smaller MOF crystals that have the same morphology as the rest of the samples. The sample histograms thus tend to be negatively skewed, with a small number of agglomerates having the largest projected areas. In Figure 2c, we plot the average crystal area obtained from the product sample histograms as a function of pH, for a reaction time of 24 h. The average crystal size is an order of magnitude larger below pH 4.0 than at higher pH values. The crossover pH (4.0) roughly corresponds to a 1:1 molar ratio between HNO_3 and the ligand precursor 3-cyanopyridine (3-py), i.e., there are protons in excess. This demonstrates the role of nitric acid as a modulator of the crystal growth process. Figure 2c also shows that the size dispersion decreases above the crossover pH. The total number of crystals in the sample (N) is smaller by an order of magnitude below pH 4.0 (Figure 2c, inset), which indicates that the growth of initial seeds is favored over the nucleation of new crystals below the crossover pH.

We study the dynamics of MIRO-101 crystal nucleation and growth by carrying out the image processing analysis described above, for reactions at the fixed pH, temperature, and ligand-to-metal molar ratio, but at variable reaction times. Figure 2d shows the average crystal areas as a function of time for pH values 2.7 and 4.0. The crystal size stabilizes after 24 h, independent of the pH used, to a long-time value that is determined by the solubility of the MOF crystal at the reaction temperature and the dilution level. Our image analysis has a lower detection threshold of 0.001 mm^2; hence, our technique is insensitive to the earliest stages of nucleation. Early nucleation can be studied with in situ XRD.[41] For pH 4.0, we detect crystallization for reaction times as early as 90 min, which correlates with the fast growth of early crystal seeds. For pH 2.7, no crystals are detected before 4 h.

We adopt the methodology used in refs 42 and 43 and define the extent of the crystallization parameter $\alpha(t)$, as the

https://doi.org/10.1021/acsomega.1c01272
ACS Omega XXXX, XXX, XXX−XXX

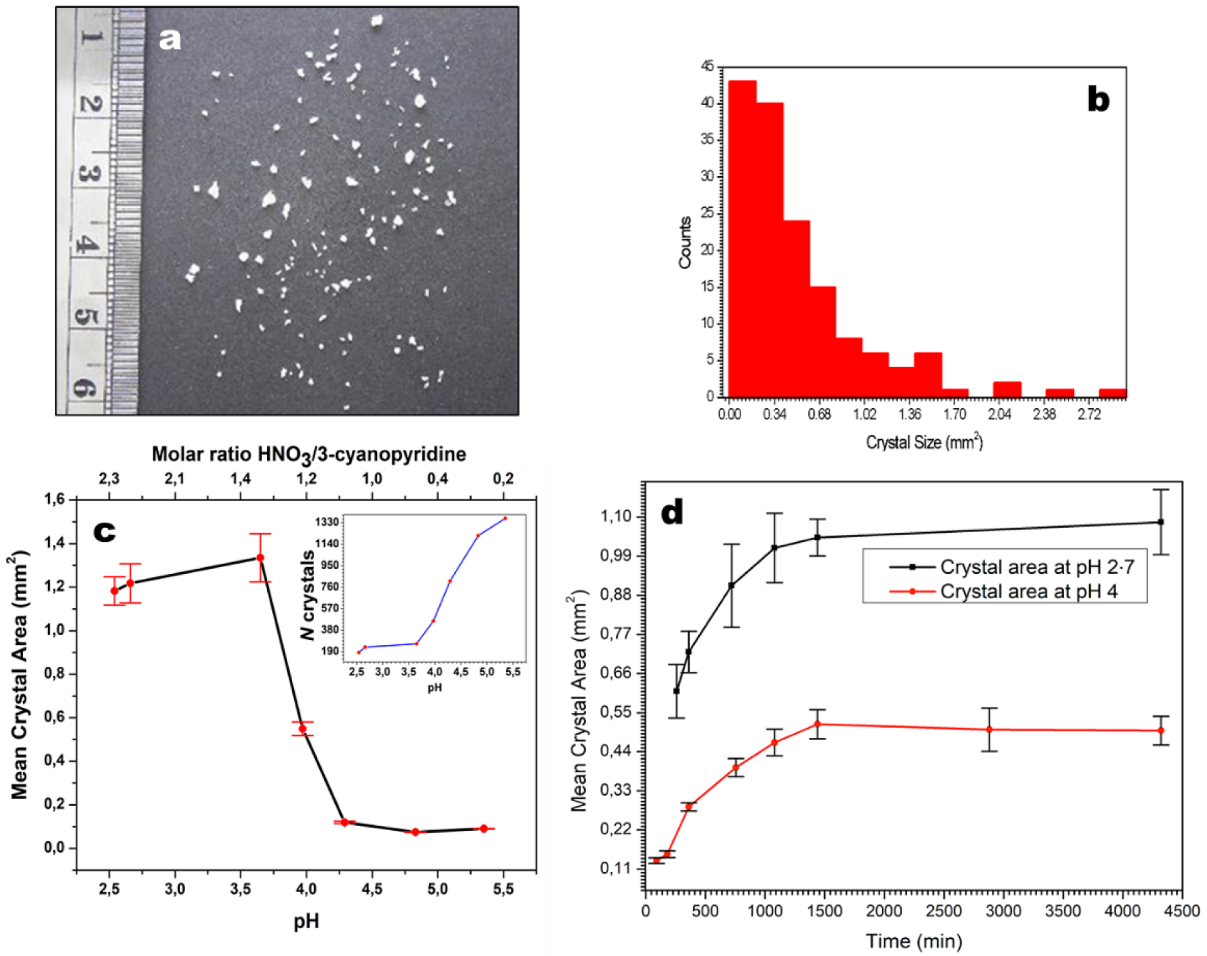

Figure 2. (a) Unprocessed crystal photograph and (b) histogram of the crystal area. Growth curve of MIRO-101 crystals at 105 °C (c) as a function of pH and/or molar ratio HNO_3/3-cyanopyridine for 24 h of reaction and (d) as a function of time at pH 4 and 2.7.

instantaneous average crystal area of a sample, normalized to the maximum average area reached after 24 h (for details, see Experimental Section). The parameter α thus varies between 0 (early times) and 1 (long times), as can be seen in Figure S1. The crystallization curves in Figure 2d were fitted to the Gualtieri model of nucleation and growth (Gualtieri fit curves are shown in Figure S1),[44] in which the extent of crystallization is given by eq 2. In Table 1, we report the kinetic parameters

Table 1. Fitted Gualtieri Kinetic Model Parameters

pH	R^2	A	B	k_n (min^{-1})	k_g (min^{-1})
2.7	0.998	93.16	388.08	0.011	0.00537
4	0.980	371.45	290.70	0.0027	0.01574

corresponding to pH 2.7 and 4.0. The growth rate k_g is lower at pH 2.7, but the nucleation rate k_n is higher than at pH 4.0. This suggests that nuclei or building units form earlier in the reaction under more acidic conditions. From the Gualtieri parameters, the estimated nucleation probability should reach its maximum under 4 h at pH 2.7, whereas at pH 4.0, the nucleation probability is optimal at about 6 h (see Figure S1).

To understand the influence of acid on the MOF growth process, we carry out a mechanistic study to identify the species involved in the formation of MIRO-101 crystals. By powder XRD analysis of crystals isolated at RT from the filtered solution after the reaction was complete, we identify the complex $\{[Zn(H_2O)_6]-(NO_3)_2-2C_6H_5N_5\}$ (MIRO-104 in Scheme 1) as a byproduct of the synthesis of MIRO-101 at pH 2.7. In contrast, MIRO-101 is the only isolated product of the synthesis at pH 4.0 after 24 h of reaction (powder XRD patterns are shown in Figures S2 and S3). This reveals that the zwitterion species 5-(pyridin-1-ium-3-yl)tetrazol-1-ide (3-Hptz) is formed in the reaction medium under acidic conditions. This is consistent with our previous report on the formation of the hexaaquazinc(II) dinitrate bis[5-(pyridinium-3-yl)tetrazol-1-ide] complex (MIRO-104) at RT, by adjusting the reaction pH to 2.0.[45] Although high acid conditions favor the formation of the MIRO-104 complex, we are still able to produce MIRO-101 crystals in the pH range of 2.1−2.5, by simply heating at 120 °C.

The formation of the zwitterion species (3-Hptz) during the assembly process of MIRO-101 is confirmed by the formation of the MIRO-104 complex under addition of 2 equiv of HNO_3 to MIRO-101. In the reverse process, MIRO-101 is formed by the addition of 2 equiv of KOH to the MIRO-104 complex (see Scheme S1 and powder XRD patterns shown in Figures S4 and S5). In addition, DFT calculations suggest that the zwitterion species (3-Hptz) is isoenergetic to the neutral 3-(1*H*-tetrazol-5-yl)pyridine (3-ptz) species, whereas anionic 5-(pyridin-3-yl)tetrazol-2-ide (ptz^-) species is the least stable by ca. 30 kcal/mol (see Figure S10).

We also analyzed the crystals formed during the first few minutes of the reaction. The MOF $[Zn(3\text{-ptz})(N_3)]_n$ (MIRO-

https://doi.org/10.1021/acsomega.1c01272
ACS Omega XXXX, XXX, XXX−XXX

Scheme 1. Plausible Mechanism for the Formation of MIRO-101 under Acidic Conditions

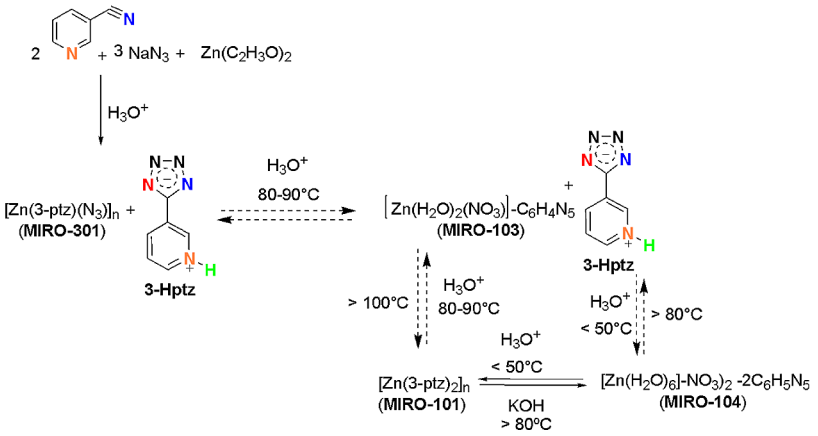

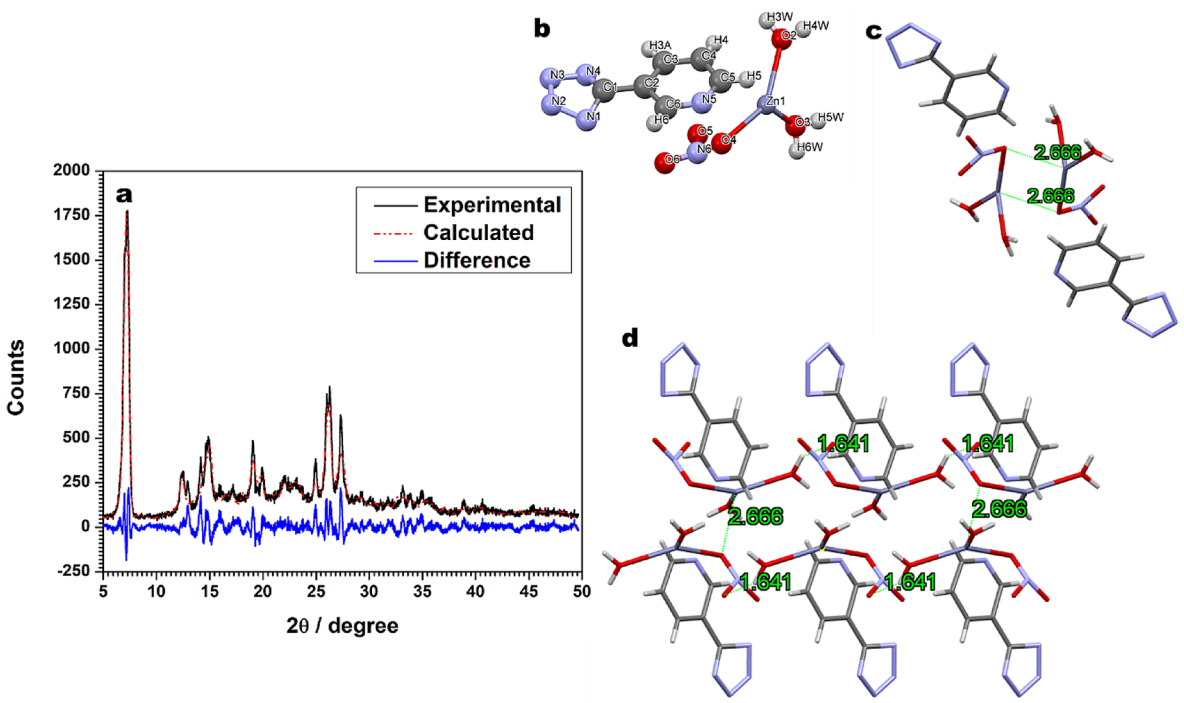

Figure 3. (a) Experimental (black), calculated (red), and difference (blue) patterns for the Rietveld refinement of the intermediate compound MIRO-103; (b) asymmetric unit of the intermediate compound MIRO-103; (c) view along the *a* axis; and (d) view along the *c* axis (green numbers are the interatomic distances in Å).

301) was isolated as pure crystals after 45 min in the synthesis of MIRO-101 at 105 °C and pH 4.0 (powder XRD patterns are shown in Figure S6). In contrast, MIRO-301 crystals were not isolated when we carried out the synthesis at pH 2.7. However, MIRO-301 is isolated as the main product when using a 1:2 molar ratio of 3-cyanopyridine and sodium azide.[38] We also found that MIRO-101 is formed by the reaction of MIRO-301 and 1 equiv of the ligand 3-pyridyltetrazole (3-ptz) (see Scheme S1 and powder XRD patterns in Figure S7). Likewise, MIRO-101 is obtained as the main product from the reaction of MIRO-301 with 1 equiv of HNO_3, but a polycrystalline solid was isolated as a byproduct when the filtered solution cools to RT. Powder XRD analysis indicated that polycrystalline solid is composed of the mixture of MIRO-101 and the intermediate compound (MIRO-103) (powder XRD patterns are shown in Figure S8).

We succeeded in isolating the intermediate compound MIRO-103 as a crystalline pure powder from the synthesis of $[Zn(3\text{-ptz})_2]_n$ at 80 °C, by adjusting the pH to 2.7. In addition, MIRO-104 becomes MOF MIRO-101 by increasing the temperature above 95 °C. Attempts to grow a sample for single-crystal XRD analysis failed. The crystal structure of MIRO-103 was determined by analyzing the powder diffraction data with the software EXPO2014 (Figure 3a; for further details, see Experimental Section).[46,47] The asymmetric unit is composed of one 5-(pyridin-3-yl)tetrazol-2-ide (ptz^-) anion and $[Zn(NO_3)(H_2O)_2]^+$ cation, which is formed by coordination to the zinc center of one nitrate ion and two water molecules for a slightly distorted planar trigonal geometry ($\Sigma\theta_{Zn}$ = 356.6°) (Figures 3b and S9).

While the Zn−O2 bond shows a typical distance (1.940 Å) for the Zn−OH2 bond, Zn−O3 shows a longer bond distance (2.506 Å).[48−50] Likewise, the nitrate ion is coordinated to zinc

https://doi.org/10.1021/acsomega.1c01272
ACS Omega XXXX, XXX, XXX−XXX

through one oxygen atom showing an elongated Zn−O bond distance (2.514 Å).[51] The nitrate ion shows a slightly distorted planar trigonal geometry ($\Sigma\theta_{Zn}$ = 352.7°) with N−O bond distances comparable to those in other reported coordinated nitrate ions (see Figure S9).[48−50] Trigonal-planar zinc(II) complexes are uncommon. Only two structures are found in the literature.[52,53] However, the 5-(pyridin-3-yl)tetrazol-2-ide (ptz^-) anion shows a strongly distorted tetrazolide ring that formed a dihedral angle of 10.4° with the pyridyl ring. Although C−C, N−C, and N−N bonds show distances comparable to those observed in the reported pyridyltetrazole compounds, the N3−N4 bond distance resulted in an untypically length (1.414 Å) as a consequence of the strong distortion of the tetrazolide ring. Finally, a dimeric structure is generated by the interaction of Zn···O4 (2.666 Å) between two $[Zn(NO_3)(H_2O)_2]^+$ units, and each dimeric fragment interacts via hydrogen bonding $O5_{nitrate}\cdots H3_{water}$ (1.641 Å) to form a 1D chain along the *a*-axis (Figure 3c,d).

Based on the experimental evidence collected, in Scheme 1, we propose a plausible mechanism for the formation of the $[Zn(3\text{-}ptz)_2]_n$ MOF. The mechanism considers the formation of $[Zn(3\text{-}ptz)(N_3)]_n$ (MIRO-301) in the early stages of reaction, whereas 3-pyridyltetrazole remains in the zwitterion form (3-Hptz). The acidic environment of the reaction medium favors the conversion from MIRO-301 to MIRO-101 through the intermediate species (MIRO-103). Increasing the reaction temperature induces the deprotonation of zwitterion species, 5-(pyridin-1-ium-3-yl)tetrazol-1-ide (3-Hptz), increasing the concentration of anionic 5-(pyridin-3-yl)tetrazol-2-ide (ptz^-) species to form $[Zn(3\text{-}ptz)_2]_n$ (MIRO-101). The remaining precursor materials crystallize at RT to form the MIRO-104 complex (Scheme 1). However, highly acidic conditions favor the protonation of anionic 5-(pyridine-3-yl)tetrazol-2-ide ($3\text{-}ptz^-$), giving MIRO-104 instead of MIRO-101. Therefore, the increase in hydronium ions limits the concentration of the precursor species involved in the formation of our target MOF (MIRO-101), giving a yield after 24 h of reaction that decreases from 80% to 28% by lowering pH from 4.0 to 2.7, respectively.

The kinetics and mechanistic studies performed on the self-assembly of MIRO-101 MOF crystals exhibit the threefold influence of solvated hydronium ions: (i) protons increase the concentration of the intermediate compound (MIRO-103) through a faster conversion from MIRO-301. This explains why we are able to isolate MIRO-301 at pH 4.0 and not at pH 2.7; (ii) in addition to the zinc salt,[35] nitric acid acts as a catalyst in the formation of the 3-pyridyltetrazol ligand. In fact, Brønsted acids (e.g., HNO_3) have been shown to have a better catalytic efficiency than zinc salts in the synthesis of tetrazole compounds via azide−nitrile cycloaddition.[54] Both effects would increase the concentration of MOF precursors, which result in higher nucleation rates at pH 2.7 (see k_n values in Table 1). Nevertheless, (iii) the increase in the hydronium ions favors the formation of the zwitterion species, 5-(pyridin-1-ium-3-yl)tetrazol-1-ide (3-Hptz), limiting the availability of the anionic species, 5-(pyridin-3-yl)tetrazol-2-ide (ptz^-). This inhibits the number of available nuclei or building units to form MIRO-101 crystals. As a consequence, the crystal growth is slow and larger-sized crystals are obtained (k_g value smaller at pH 2.7 than at pH 4.0; see Table 1). This result contrasts to those reported for MOF based on carboxylic linkers, in which the growth of larger-sized crystals is attributed to a lower extent of the deprotonation of ligands under acidic conditions.[32,33]

The above results reveal that the reaction pH is one of key control parameters to achieve an optimum MIRO-101 crystal size. Building on this understanding, we aim to grow large-sized single crystals by adjusting the reaction pH to 2.7 and carefully controlling the temperature using a tubular muffle furnace. Finally, we have achieved the growth of a single $[Zn(3\text{-}ptz)_2]_n$ crystal with a diameter ∼6 mm after 24 h of reaction at 105 °C by using a tubular muffle furnace (Figure 1a). The tubular muffle allows uniform heating around a home-built glass reaction vessel, designed with a width close to the internal diameter of the tubular muffle, in order to decrease temperature fluctuations by conduction heating.

Building on previous work,[37] we tested alternative inorganic acids in an effort to increase the crystalline quality of the $[Zn(3\text{-}ptz)_2]_n$ crystals produced at low pH, without observing significant changes in comparison with the use of nitric acid. The results, however, were significantly different when acetic acid was used as an additive. By adding an excess amount of acetic acid to the reaction mixture and then by fixing the pH to 2.7 using nitric acid (for detailed conditions, see Experimental Section), the crystal habit of $[Zn(3\text{-}ptz)_2]_n$ is significantly distorted relative to the octahedron predicted by the Bravais−Friedel−Donnay−Harker model (Figure 4a), which is the only

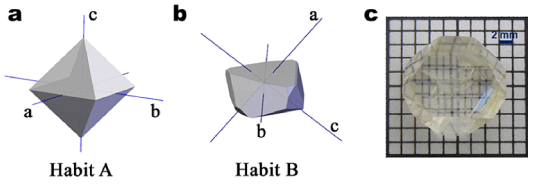

Figure 4. Modification of MIRO-101 crystal habit using zinc acetate. (a) Octahedron (habit A) with axial optical *c*-axis; (b) distorted octahedron crystal slab (habit B), with parallel hexagonal and triangular faces; and (c) optical image of the crystal sample corresponding to panel (b).

crystal habit obtained at pH 4.0.[36] Figure 4b shows the distorted single-crystal habit of a representative sample obtained at pH 2.7 in the presence of excess acetic acid.

The single-crystal XRD shows that the unit cell parameters remain unchanged relative to the regular octahedron ($a = b$ = 10.139(1) Å, c = 13.630(4) Å, $\alpha = \beta = \gamma$ = 90°), but the indexation of the faces exhibits additional planes that have higher Miller indices (see Table 2). In general, crystal habits with higher Miller indices tend to have higher surface energies;[55,56] however, understanding the detailed role of acetic acid in the self-assembly mechanism of the MOF $[Zn(3\text{-}ptz)_2]_n$ requires further computational and spectroscopic studies. These conditions allow the synthesis of high-quality single crystals, improving the *R*-factor from 3.1% to 1.1% (see crystallographic data in Table S3). Taking into account the number of MOF crystals reported in CCDC to date, only about 0.05% of the structures have reached this precision quality.

EXPERIMENTAL SECTION

Materials. All reactants and chemicals were purchased from Sigma-Aldrich and utilized without any further purification, except 3-cyanopyridine, which was sublimated at 60 °C. pH was measured with a pH meter 2700 Oakton. Powder XRD

https://doi.org/10.1021/acsomega.1c01272
ACS Omega XXXX, XXX, XXX−XXX

Table 2. Miller Indices of $[Zn(3\text{-ptz})_2]_n$ Single Crystals in Habits A and B

N	habit A	habit B
1	(1 0 1)	(1 0 1)
2	(1 0 −1)	(1 0 −1)
3	(−1 01)	(−1 0 1)
4	(−1 0 −1)	(−1 0 −1)
5	(0 1 −1)	(0 1 −1)
6	(0 −1 1)	(0 −1 1)
7	(0 −1 −1)	(0 −1 −1)
8	(0 1 1)	(0 2 −1)
9		(0 −2 1)
10		(0 −2 −1)
11		(1 0 0)
12		(1 0 2)
13		(1 1 2)
14		(−1 1 2)
15		(−1 1 −2)
16		(−1 −1 0)
17		(−1 −1 −2)
18		(−1 −2 0)
19		(2 2 1)
20		(−2 2 −1)
21		(−2 0 −1)

analysis was performed using an X Shimadzu XRD 6000 diffractometer with Cu Kα (λ = 1.5418 Å) radiation for structural characterization and phase determination. Digital camera Nikon Coolpix L610 was used for photographing the as-synthesized crystals. While the tubular furnace Nabertherm (model no. 50-250/11) was used in the synthesis of large single MIRO-101 crystals, a box furnace was employed for crystallization kinetic studies.

Methods. *Procedure for the Preparation of Large-Sized MIRO-101 with Crystal Habit A.* A mixture of $Zn(CH_3COO)_2$ (2 mmol), 3-cyanopyridine (4 mmol), and sodium azide (6 mmol) was dissolved in 6 mL of distilled water in a 25 mL glass bottle, and the reaction pH was adjusted to 2.7 using HNO_3 (70%). The glass bottle was introduced into a tubular furnace at 105 °C for 24 h using a horizontal operation, and the furnace was filled with alumina bulk fiber for preventing temperature fluctuations. The as-synthesized crystals were filtered immediately after the completion of the reaction and washed using a mixture of water/ethanol and dried at RT.

Procedure for the Preparation of Large-Sized MIRO-101 with Crystal Habit B. A mixture of $Zn(CH_3COO)_2$ (3.26 mmol), 3-cyanopyridine (6.52 mmol), sodium azide (9.78 mmol), and acetic acid (3.26 mmol) was dissolved in 14 mL of distilled water in a glass bottle of 50 mL, and the pH value was adjusted to 2.7 using HNO_3 (70%). The glass bottle was introduced into a tubular furnace at 105 °C for 40 h using a horizontal operation, and the furnace was filled with alumina bulk fiber. The as-synthesized crystals were filtered immediately after the completion of the reaction and washed using a mixture of water/ethanol and dried at RT.

Crystallization Kinetics Study. *General Procedure.* MIRO-101 crystals were synthesized as described above, by adjusting the reaction pH at both 2.7 and 4.0. For this study, the glass bottle was introduced into a box furnace at 105 °C at different reaction times. The crystals were photographed, and the crystalline purity was confirmed by powder XRD. However, colorless crystals were isolated at RT from a filtered solution. These crystals were washed with water, dried, and analyzed by powder XRD.

Crystal Size Quantification. Due to the large size of the synthesized crystals, estimating their sizes using both optical and scanning electron microscopes was not possible. We thus estimate the area of crystals by processing pictures taken with a conventional digital camera (see Figure 2a). The crystals were placed on the dark surface and photographs were taken in high angle shots. The crystal area was measured using the program ImageJ,[57] obtaining for each photograph the following parameters: scale, threshold, minimum area, and maximum area. Once we have these values, the process is reproducible, and the images can be processed through a script written for ImageJ. The script (*img_processing.ijm*) takes the original images and generates the csv and processed images required to make the data analysis, plots, and histograms.

We found that MIRO-101 crystallized as regular-sized single crystals and octahedral in shape; however, some large-sized crystal clusters are formed by the agglomeration of single crystals. This gives bimodal size distributions. Single crystals and agglomerated single crystals can be clearly differentiated with an optical microscope, as in the agglomerated ones, the crystal boundaries of various single crystals are clearly visible. During crystal size analysis, we did not do any differentiation between single and agglomerated crystals. We just considered the whole crystal sample obtained after each experiment and the size was estimated as the average area of the crystals. We believe that this methodology provides reliable data to study the crystallization kinetics of millimeter-sized crystals, thus avoiding grinding procedures involved in XRD-based procedures for estimating crystal growth kinetics.[42] Image processing also avoids potential artifacts introduced by in situ X-ray beams on the crystallization process.[58,59]

Data Analysis. Crystallization curves at pH 4 and 2.7 were built by plotting the extent of crystallization (α) as a function of time. The extent of crystallization $[\alpha(t)]$ results from the normalization of the average area values with respect to the highest area for each experiment, i.e.,

$$\alpha(t) = \frac{\text{average area } (t)}{\text{average area maximum}} \tag{1}$$

The crystallization curves were also fitted using the Gualtieri model,[44] which separately considers the influence of nucleation and growth processes in the extent of crystallization as

$$\alpha(t) = \frac{[1 - e^{-(k_g t)^m}]}{\{1 + e^{[(t-a)/b]}\}} \tag{2}$$

where m is the dimensionality of the crystal growth. We assume the three-dimensional growth of $[Zn(3\text{-ptz})_2]_n$ crystals (m = 3), given the octahedral habits obtained. k_g is the rate constant of the crystal growth and a and b are the time constants related to the nucleation process. The rate constant for nucleation k_n is given by

$$k_n = \frac{1}{a} \tag{3}$$

In Gualtieri's model, the probability that N crystallization nuclei develop at time t is a Gaussian distribution given by

$$P_N = \frac{dN}{dt} = e^{-[(t-a)^2/2b^2]} \tag{4}$$

https://doi.org/10.1021/acsomega.1c01272
ACS Omega XXXX, XXX, XXX−XXX

The time constant a thus yields the time of the maximum nucleation rate, while b defines the distribution of the probability of nucleation with time.[44] Crystallization curves were fitted to Gaultieri's kinetic model using the standard software OriginPro 8.5, and kinetic parameters were determined by nonlinear least-squares fitting.

Reaction Tests. *Synthesis of Intermediate Compound $[Zn(H_2O)_2(NO_3)]-C_6H_4N_5$ (MIRO-103).* A mixture of 3-cyanopyridine (4 mmol), NaN_3 (6 mmol), and $Zn(CH_3COO)_2$ (2 mmol) was dissolved in 6 mL of distilled water in a 20 mL glass bottle. Immediately after mixing the reactants, the pH of the solution (initial pH) was adjusted to 2.7 by the addition of HNO_3 (70%) solution. The glass bottle was then capped tightly with a screw cap before being placed in a box furnace at 80 °C. A crystalline powder was formed 3 h after the starting materials were dissolved. This crystalline powder was filtered from a hot solution, washed with a water mixture, dried at RT, and analyzed by powder XRD.

Addition of HNO_3 to MIRO-101. To a solution of MIRO-101 (1 mmol) in 6 mL of distilled water, 2.1 mmol of HNO_3 (70%) solution was added. The reaction mixture was placed in a box furnace at 105 °C for 24 h. Then, it was removed from the oven and the crystals grew at RT. The as-synthesized crystals were filtered, dried, and analyzed by powder XRD.

Addition of KOH to $\{[Zn(H_2O)_6]-(NO_3)_2-2C_6H_5N_5\}$ (MIRO-104). To a solution of MIRO-104 (1 mmol) in 6 mL of distilled water, 2 mmol of KOH (6 M) solution was added. The reaction mixture was placed in a box furnace at 105 °C for 24 h. Then, it was removed from the oven, and the as-synthesized crystals were filtered from the hot solution, washed with a water/ethanol mixture, dried at RT, and analyzed by powder XRD.

Addition of HNO_3 to $[Zn(3\text{-ptz})(N_3)]_n$ (MIRO-301). To a solution of MIRO-301 (0.80 mmol) in 6 mL of distilled water, 0.4 mmol of HNO_3 (70%) solution was added. The reaction mixture was placed in a box furnace at 105 °C for 24 h. Then, it was removed from the oven, and the as-synthesized crystals were filtered from the hot solution, washed with a water/ethanol mixture, dried at RT, and analyzed by powder XRD. Once the filtered solution cools to RT, a byproduct precipitated as a crystalline powder, which was analyzed by powder XRD.

Reaction of 5-(3-Pyridyl)tetrazole with MIRO-301. To a mixture of MIRO-301 (0.80 mmol) and 5-(3-pyridyl)tetrazole (0.8 mmol), 6 mL of distilled water was added. Immediately after mixing the reactants, the pH of the solution was measured as 3.6. The reaction mixture was placed in a box furnace at 105 °C for 24 h. Then, it was removed from the oven, and the as-synthesized crystals were filtered from the hot solution, washed with a water/ethanol mixture, dried at RT, and analyzed by powder XRD.

Structural Characterization of MIRO-103. The crystal structure of the intermediate compound MIRO-103 was solved by analyzing powder XRD data. We first attempted to find the cell parameters by autoindexing using the algorithms DICVOL and TREOR;[60,61] unfortunately, nonsolutions were found. Then, we used the cell parameters and space group of the MIRO-104 complex, i.e., a = 5.6582 Å, b = 8.4632 Å, c = 12.046 Å, α = 97.209°, β = 91.123°, γ = 93.949°, and P-1.[45] We tried to solve the structure by simulated annealing using the crystal structure of the complex (MIRO-104). Unfortunately, all solutions showed chemically unreasonable coordination patterns. Finally, we solved the structure by simulated annealing using (i) one deprotonated 3-pyridyltetrazol molecule (3-ptz$^-$), (ii) one $[Zn(H_2O)_2]^{2+}$ fragment, and (iii) one nitrate ion. We performed 10 runs with 10^7 maximum number of moves for each trial, and the best solution was chosen for the Rietveld refinement. Rietveld refinements were performed using software EXPO2014.[47] The background was modeled using a Chebyshev polynomial of degree 15 and the pseudo-Voigt function was used to fit the peak shape. Restraints were imposed on bond distances and angles of fragments. The refinement converged to agreement indices χ^2 = 4.629, R_p = 12.58%, R_{wp} = 15.87%, R_{Bragg} = 4.54%, and $R_{structure}$ = 4.68%. The experimental, calculated, and difference plots are shown in Figure 3, and the miscellaneous data of the refinement are shown in Table S1.

Theoretical Calculations. The relative stability of the ligand species was computed by optimizing their structures using the DFT-based software package DMol^3.[47−49] The calculations were performed using the well-known B3LYP functional and the double-zeta plus (DNP) numerical basis set.[47−49] This basis set provides good accuracy at a relatively low computational cost. The all-electron core treatment was applied to all of the atoms. All calculations were performed by considering an implicit solvent treatment under the conductor-like screening for the realistic solvent model (COSMO-RS) approach. A dielectric constant of 78.54 for water at 298.15 K was used. This model was chosen owing to its relative computational efficiency, which allows it to be incorporated into every step of the structure optimization process without increasing the computational cost appreciably. Frequency calculations were computed to confirm that the optimized structures correspond to energy minima on the potential energy surface, and thermal corrections for energy and entropy were done at 298.15 K to obtain the free energies.

Determination of the Plane of Crystal Faces. The planes of crystal faces were characterized by indexing the planes in a SMART CCD diffractometer using the orientation matrix. The coordinates of the vertices were obtained in the KrystalShaper software (http://www.jcrystal.com/products/krystalshaper) using the values of the orientation matrix and exporting the crystal shape in a VRML2 file. The representation of the crystal habits and planes was done using the software WinX-Morph.[62,63] The surface and crystal volume for habit B were calculated using the AlphaShape code provided on the Matlab.

CONCLUSION

In this work, we propose a plausible mechanism for the formation of the MOF $[Zn(3\text{-ptz})_2]_n$ (MIRO-101), by isolating and identifying a number of crystal structures involved in the self-assembly process under acidic conditions. Using powder XRD analysis, we determine the crystal structure of the reaction intermediate $[Zn(H_2O)_2(NO_3)]-C_6H_4N_5$ complex (MIRO-103), which we isolate at 80 °C. We elucidate the detailed role of pH in the growth process of the target MOF crystal. An ex situ analysis of a large number of crystal images is used to carry out a crystallization kinetics study that demonstrates an increase in the crystal nucleation rate with the simultaneous decrease in the crystal growth rate for pH values below 4.0. By controlling the synthetic parameters, such as molar ratio, pH and temperature, we report large single crystals of MIRO-101 with surface areas of approximately 25 mm^2, grown as the main product of a single solvothermal reaction with in situ ligand formation. No postsynthetic growth or cooling steps are needed to obtain

https://doi.org/10.1021/acsomega.1c01272
ACS Omega XXXX, XXX, XXX−XXX

large crystal sizes. These unprecedented crystal dimensions are obtained under highly acidic reaction conditions that favors the protonation of anionic 5-(pyridine-3-yl)tetrazol-2-ide (3-ptz$^-$), limiting the concentration of precursor species involved in the formation of MIRO-101. This, in turn, slows the growth process, favoring the formation of larger-sized crystals.

Further, several properties of the large-sized crystal (habit A and habit B) will be studied, such as crystallinity, transmittance, and stability, in due course of time, and the results will be a part of the forthcoming article. Since the most important and preliminary stage in the process to see the possible SHG was the controlled growth of millimeter-sized single crystals, this work is an achievement in that direction, which reports overcoming of the large-sized crystal issue. The next goal is the nonlinear optics behavior, such as the SHG of millimeter-sized MIRO-101 single crystals, which is still unexplored.[40] Therefore, this crystal growth work represents a step in the development of MOF-based crystal devices for envisioned applications in classical and quantum optics.

■ ASSOCIATED CONTENT

Supporting Information

The Supporting Information is available free of charge at https://pubs.acs.org/doi/10.1021/acsomega.1c01272.

Crystallographic data and X-ray analysis, theoretical calculations, Rietveld refinement data, and crystallization kinetics analysis are shown in the supporting information (PDF)

■ AUTHOR INFORMATION

Corresponding Authors

Felipe Herrera − *Physics Department, Faculty of Science, University of Santiago of Chile (USACH), Santiago, Estación Central 9170124, Chile; ANID − Millennium Science Initiative Program, Millennium Institute for Research in Optics, San Pedro de la Paz, Concepción 4130691, Chile;* orcid.org/0000-0001-8121-1931; Email: felipe.herrera.u@usach.cl

Dinesh P. Singh − *Physics Department, Faculty of Science, University of Santiago of Chile (USACH), Santiago, Estación Central 9170124, Chile; ANID − Millennium Science Initiative Program, Millennium Institute for Research in Optics, San Pedro de la Paz, Concepción 4130691, Chile;* orcid.org/0000-0002-2893-7749; Email: dineshpsingh@gmail.com, singh.dinesh@usach.cl

Authors

Juan M. Garcia-Garfido − *Physics Department, Faculty of Science, University of Santiago of Chile (USACH), Santiago, Estación Central 9170124, Chile; ANID − Millennium Science Initiative Program, Millennium Institute for Research in Optics, San Pedro de la Paz, Concepción 4130691, Chile*

Javier Enríquez − *Physics Department, Faculty of Science, University of Santiago of Chile (USACH), Santiago, Estación Central 9170124, Chile; Department of Metallurgical Engineering, Faculty of Engineering, University of Santiago, Chile, Santiago, Estación Central 9170022, Chile;* orcid.org/0000-0002-2502-5787

Ignacio Chi-Durán − *Physics Department, Faculty of Science, University of Santiago of Chile (USACH), Santiago, Estación Central 9170124, Chile; ANID − Millennium Science Initiative Program, Millennium Institute for Research in Optics, San Pedro de la Paz, Concepción 4130691, Chile;* orcid.org/0000-0002-3327-2825

Iván Jara − *Physics Department, Faculty of Science, University of Santiago of Chile (USACH), Santiago, Estación Central 9170124, Chile*

Leonardo Vivas − *Physics Department, Faculty of Science, University of Santiago of Chile (USACH), Santiago, Estación Central 9170124, Chile; ANID − Millennium Science Initiative Program, Millennium Institute for Research in Optics, San Pedro de la Paz, Concepción 4130691, Chile*

Federico J. Hernández − *Department of Chemistry, School of Biological and Chemical Sciences, Queen Mary University of London, London E1 4NS, U.K.*

Complete contact information is available at: https://pubs.acs.org/10.1021/acsomega.1c01272

Notes

The authors declare no competing financial interest.

■ ACKNOWLEDGMENTS

This work was funded by the ANID − Millennium Science Initiative Program (no. ICN17_012). The authors thank Andrés Vega and Daniel Serafini for support with crystallography. F.H. was supported by ANID − FONDECYT Regular no. 1181743.

■ REFERENCES

(1) Li, H.; Wang, K.; Sun, Y.; Lollar, C. T.; Li, J.; Zhou, H. C. Recent Advances in Gas Storage and Separation Using Metal−Organic Frameworks. *Mater. Today* **2018**, *21*, 108−121.

(2) Hu, Y.; Lin, B.; He, P.; Li, Y.; Huang, Y.; Song, Y. Probing the Structural Stability of and Enhanced CO_2 Storage in MOF MIL-68(In) under High Pressures by FTIR Spectroscopy. *Chem. - Eur. J.* **2015**, *21*, 18739−18748.

(3) Li, X.; Liu, Y.; Wang, J.; Gascon, J.; Li, J.; Van Der Bruggen, B. Metal−Organic Frameworks Based Membranes for Liquid Separation. *Chem. Soc. Rev.* **2017**, *46*, 7124−7144.

(4) Li, Y.; Zou, B.; Xiao, A.; Zhang, H. Advances of Metal-Organic Frameworks in Energy and Environmental Applications. *Chin. J. Chem.* **2017**, *35*, 1501−1511.

(5) Gao, X.; Hai, X.; Baigude, H.; Guan, W.; Liu, Z. Fabrication of Functional Hollow Microspheres Constructed from MOF Shells: Promising Drug Delivery Systems with High Loading Capacity and Targeted Transport. *Sci. Rep.* **2016**, *6*, No. 37705.

(6) Ibrahim, M.; Sabouni, R.; Husseini, G. A. Synthesis of Metal-Organic Framework from Iron Nitrate and 2,6-Naphthalenedicarboxylic Acid and Its Application as Drug Carrier. *J. Nanosci. Nanotechnol.* **2018**, *18*, 5266−5273.

(7) Remya, V. R.; Kurian, M. Synthesis and Catalytic Applications of Metal−Organic Frameworks: A Review on Recent Literature. *Int. Nano Lett.* **2019**, *9*, 17−29.

(8) Müller-Buschbaum, K.; Beuerle, F.; Feldmann, C. MOF Based Luminescence Tuning and Chemical/Physical Sensing. *Microporous Mesoporous Mater.* **2015**, *216*, 171−199.

(9) Yi, F.-Y.; Chen, D.; Wu, M.-K.; Han, L.; Jiang, H.-L. Chemical Sensors Based on Metal-Organic Frameworks. *ChemPlusChem* **2016**, *81*, 675−690.

(10) Vittal, J. J.; Chen, Z. J.; Gallo, G.; Sawant, V. A.; Zhang, T. J.; Zhu, M. J.; Liang, L. J.; Chanthapally, A. J.; Bolla, G. J.; Quah, H. S.; Liu, X. J.; Loh, K. P.; Dinnebier, R. E.; Xu, Q.-H. J. Giant Enhancement of Second Harmonic Generation Accompanied by the Structural Transformation of 7-Fold to 8-Fold Interpenetrated MOF. *Angew. Chem., Int. Ed.* **2020**, *59*, 833−838.

(11) Mingabudinova, L. R.; Vinogradov, V. V.; Milichko, V. A.; Hey-Hawkins, E.; Vinogradov, A. V. Metal−Organic Frameworks as

Competitive Materials for Non-Linear Optics. *Chem. Soc. Rev.* **2016**, *45*, 5408−5431.
(12) Wang, C.; Zhang, T.; Lin, W. Rational Synthesis of Noncentrosymmetric Metal-Organic Frameworks for Second-Order Nonlinear Optics. *Chem. Rev.* **2012**, *112*, 1084−1104.
(13) Yang, X.; Lin, X.; Zhao, Y. S.; Yan, D. Recent Advances in Micro-/Nanostructured Metal−Organic Frameworks towards Photonic and Electronic Applications. *Chem. - Eur. J.* **2018**, *24*, 6484−6493.
(14) Mendiratta, S.; Lee, C.-H.; Usman, M.; Lu, K.-L. Metal−Organic Frameworks for Electronics: Emerging Second Order Nonlinear Optical and Dielectric Materials. *Sci. Technol. Adv. Mater.* **2015**, *16*, No. 054204.
(15) Yang, L.; Yang, N.; Li, B. Extreme Low Thermal Conductivity in Nanoscale 3D Si Phononic Crystal with Spherical Pores. *Nano Lett.* **2014**, *14*, 1734−1738.
(16) Demos, S. G.; DeMange, P.; Negres, R. A.; Feit, M. D. Investigation of the Electronic and Physical Properties of Defect Structures Responsible for Laser-Induced Damage in DKDP Crystals. *Opt. Express* **2010**, *18*, No. 13788.
(17) Kwiat, P. G.; Waks, E.; White, A. G.; Appelbaum, I.; Eberhard, P. H. Ultrabright Source of Polarization-Entangled Photons. *Phys. Rev. A* **1999**, *60*, R773−R776.
(18) Boyd, R. *Nonlinear Optics − 3rd Edition*. Academic Press, 2008; https://www.elsevier.com/books/nonlinear-optics/boyd/978-0-12-369470-6 (accessed 2020-08-3).
(19) Wang, L. Z.; Qu, Z. R.; Zhao, H.; Wang, X.-S.; Xiong, R. G.; Xue, Z. L. Isolation and Crystallographic Characterization of a Solid Precipitate/Intermediate in the Preparation of 5-Substituted 1H-Tetrazoles from Nitrile in Water. *Inorg. Chem.* **2003**, *42*, 3969−3971.
(20) Ok, K. M.; Chi, E. O.; Halasyamani, P. S. Bulk Characterization Methods for Non-Centrosymmetric Materials: Second-Harmonic Generation, Piezoelectricity, Pyroelectricity, and Ferroelectricity. *Chem. Soc. Rev.* **2006**, *35*, 710−717.
(21) Colón, Y. J.; Guo, A. Z.; Antony, L. W.; Hoffmann, K. Q.; De Pablo, J. J. Free Energy of Metal-Organic Framework Self-Assembly. *J. Chem. Phys.* **2019**, *150*, No. 104502.
(22) Liu, B.; Vellingiri, K.; Jo, S. H.; Kumar, P.; Ok, Y. S.; Kim, K. H. Recent Advances in Controlled Modification of the Size and Morphology of Metal-Organic Frameworks. *Nano Res.* **2018**, *11*, 4441−4467.
(23) Uemura, T.; Hoshino, Y.; Kitagawa, S.; Yoshida, K.; Isoda, S. Effect of Organic Polymer Additive on Crystallization of Porous Coordination Polymer. *Chem. Mater.* **2006**, *18*, 992−995.
(24) Sun, Y.; Amsler, M.; Goedecker, S.; Caravella, A.; Yoshida, M.; Kato, M. Surfactant-Assisted Synthesis of Large Cu-BTC MOF Single Crystals and Their Potential Utilization as Photodetectors. *CrystEngComm* **2019**, *21*, 3949−3953.
(25) Pan, Y.; Heryadi, D.; Zhou, F.; Zhao, L.; Lestari, G.; Su, H.; Lai, Z. Tuning the Crystal Morphology and Size of Zeolitic Imidazolate Framework-8 in Aqueous Solution by Surfactants. *CrystEngComm* **2011**, *13*, 6937−6940.
(26) Guo, H.; Zhu, Y.; Wang, S.; Su, S.; Zhou, L.; Zhang, H. Combining Coordination Modulation with Acid−Base Adjustment for the Control over Size of Metal−Organic Frameworks. *Chem. Mater.* **2012**, *24*, 444−450.
(27) Liu, Y.; Gao, P.; Huang, C.; Li, Y. Shape- and Size-Dependent Catalysis Activities of Iron-Terephthalic Acid Metal-Organic Frameworks. *Sci. China Chem.* **2015**, *58*, 1553−1560.
(28) Guo, H.; Zhu, Y.; Qiu, S.; Lercher, J. A.; Zhang, H. Coordination Modulation Induced Synthesis of Nanoscale $Eu_{1-x}Tbx$−Metal−Organic Frameworks for Luminescent Thin Films. *Adv. Mater.* **2010**, *22*, 4190−4192.
(29) Wang, Y.; Yang, H. Oleic Acid as the Capping Agent in the Synthesis of Noble Metal Nanoparticles in Imidazolium-Based Ionic Liquids. *Chem. Commun.* **2006**, 2545−2547.
(30) Schaate, A.; Roy, P.; Godt, A.; Lippke, J.; Waltz, F.; Wiebcke, M.; Behrens, P. Modulated Synthesis of Zr-Based Metal−Organic Frameworks: From Nano to Single Crystals. *Chem. - Eur. J.* **2011**, *17*, 6643−6651.
(31) Diring, S.; Furukawa, S.; Takashima, Y.; Tsuruoka, T.; Kitagawa, S. Controlled Multiscale Synthesis of Porous Coordination Polymer in Nano/Micro Regimes. *Chem. Mater.* **2010**, *22*, 4531−4538.
(32) Han, S.; Wei, Y.; Valente, C.; Lagzi, I.; Gassensmith, J. J.; Coskun, A.; Stoddart, J. F.; Grzybowski, B. A. Chromatography in a Single Metal−Organic Framework (MOF) Crystal. *J. Am. Chem. Soc.* **2010**, *132*, 16358−16361.
(33) Li, L.; Sun, F.; Jia, J.; Borjigin, T.; Zhu, G. Growth of Large Single MOF Crystals and Effective Separation of Organic Dyes. *CrystEngComm* **2013**, *15*, 4094−4098.
(34) Hu, Z.; Castano, I.; Wang, S.; Wang, Y.; Peng, Y.; Qian, Y.; Chi, C.; Wang, X.; Zhao, D. Modulator Effects on the Water-Based Synthesis of Zr/Hf Metal−Organic Frameworks: Quantitative Relationship Studies between Modulator, Synthetic Condition, and Performance. *Cryst. Growth Des.* **2016**, *16*, 2295−2301.
(35) Demko, Z. P.; Sharpless, K. B. Preparation of 5-Substituted 1H-Tetrazoles from Nitriles in Water. *J. Org. Chem.* **2001**, *66*, 7945−7950.
(36) Chi-Duran, I.; Enríquez, J.; Manquian, C.; Wrighton-Araneda, K.; Cañon-Mancisidor, W.; Venegas-Yazigi, D.; Herrera, F.; Singh, D. P. pH-Controlled Assembly of 3D and 2D Zinc-Based Metal-Organic Frameworks with Tetrazole Ligands. *ACS Omega* **2018**, *3*, 801−807.
(37) Enríquez, J.; Manquian, C.; Chi-Duran, I.; Herrera, F.; Singh, D. P. Controlled Growth of the Noncentrosymmetric Zn(3-Ptz) 2 and Zn(OH)(3-Ptz) Metal−Organic Frameworks. *ACS Omega* **2019**, *4*, 7411−7419.
(38) Chi-duran, I.; Enríquez, J.; Manquián, C.; Fritz, R. A.; Vega, A.; Serafini, D.; Herrera, F.; Singh, D. P. Azide-Based High-Energy Metal−Organic Frameworks with Enhanced Thermal Stability. *ACS Omega* **2019**, *4*, 14398−14403.
(39) Chi-Duran, I.; Enriquez, J.; Vega, A.; Herrera, F.; Singh, D. P. Hexaaquazinc(II) Dinitrate Bis[5-(pyridinium-3-Yl)tetrazol-1-ide]. *Acta Crystallogr., Sect. E: Crystallogr. Commun.* **2018**, *74*, 1231−1234.
(40) Chi-Duran, I.; Fritz, R.; Olaya, V.; Urzua-Leiva, R.; Cárdenas-Jirón, G. I.; Singh, D. P.; Herrera, F. Anisotropic Band-Edge Absorption of Millimeter-Size $Zn(3\text{-}Ptz)_2$ Single Crystal Metal-Organic Frameworks. 2020. DOI: 10.26434/CHEMRXIV.13370414.V1
(41) Millange, F.; Medina, M. I.; Guillou, N.; Férey, G.; Golden, K. M.; Walton, R. I. Time-Resolved in Situ Diffraction Study of the Solvothermal Crystallization of Some Prototypical Metal−Organic Frameworks. *Angew. Chem., Int. Ed.* **2010**, *49*, 763−766.
(42) Haque, E.; Jeong, J. H.; Jhung, S. H. Synthesis of Isostructural Porous Metal-Benzenedicarboxylates: Effect of Metal Ions on the Kinetics of Synthesis. *CrystEngComm* **2010**, *12*, 2749−2754.
(43) Moreno-Cencerrado, A.; Iturri, J.; Toca-Herrera, J. L. In-situ 2D bacterial crystal growth as a function of protein concentration: An atomic force microscopy study. *Microsc. Res. Tech.* **2018**, *81*, 1095−1104.
(44) Gualtieri, A. F. Synthesis of Sodium Zeolites from a Natural Halloysite. *Phys. Chem. Miner.* **2001**, *28*, 719−728.
(45) Chi-duran, I.; Enriquez, J.; Vega, A.; Herrera, F.; Singh, D. P. Hexaaquazinc (II) Dinitrate Bis[5-(Pyridinium-3-yl)tetrazol-1-ide]. *Acta Crystallogr., Sect. E: Struct. Rep. Online* **2018**, *74*, 1231−1234.
(46) Altomare, A.; Corriero, N.; Cuocci, C.; Falcicchio, A.; Moliterni, A.; Rizzi, R. EXPO Software for Solving Crystal Structures by Powder Diffraction Data: Methods and Application. *Cryst. Res. Technol.* **2015**, *50*, 737−742.
(47) Altomare, A.; Cuocci, C.; Giacovazzo, C.; Moliterni, A.; Rizzi, R.; Corriero, N.; Falcicchio, A. EXPO2013: A Kit of Tools for Phasing Crystal Structures from Powder Data. *J. Appl. Crystallogr.* **2013**, *46*, 1231−1235.
(48) Ghosh, D.; Lebedyte, I.; Yufit, D. S.; Damodaran, K. K.; Steed, J. W. Selective Gelation of N-(4-Pyridyl)Nicotinamide by Copper(II) Salts. *CrystEngComm* **2015**, *17*, 8130−8138.

https://doi.org/10.1021/acsomega.1c01272
ACS Omega XXXX, XXX, XXX−XXX

(49) Dong, Y.; Cheng, J. Y.; Wang, H. Y.; Huang, R. Q.; Tang, B.; Smith, M. D.; Zur Loye, H. C. New Coordination Polymers and Supramolecular Complexes Generated from Oxadiazole-Containing Organic Ligands and Inorganic M(II) (M = Zn and Cu) Salts. *Chem. Mater.* **2003**, *15*, 2593−2604.
(50) Barnett, S. A.; Blake, A. J.; Champness, N. R.; Wilson, C. Using Simple Aquo Complexes and Sterically Hindered Aromatic N-Donor Ligands to Generate Hydrogen-Bonded Frameworks. *J. Supramol. Chem.* **2002**, *2*, 17−20.
(51) Suriya Narayanan, R.; Chandrasekhar, V. Molecular, 1D and 2D Assemblies from Hexakis(3-Pyridyloxy)Cyclophosphazene Containing 20-Membered Metallamacrocyclic Motifs. *Dalton Trans.* **2016**, *45*, 2273−2283.
(52) Kunert, M.; Bräuer, M.; Klobes, O.; Görls, H.; Dinjus, E.; Anders, E. Carboxylation of Acetophenone with Zinc(II) Alkoxides/CO_2 Systems: A Mechanistic Study. *Eur. J. Inorg. Chem.* **2000**, *2000*, 1803−1809.
(53) Darensbourg, D. J.; Niezgoda, S. A.; Draper, J. D.; Reibenspies, J. H. Trigonal-Planar Zinc(II) and Cadmium(II) Tris(Phenoxide) Complexes. *Inorg. Chem.* **1999**, *38*, 1356−1359.
(54) Cantillo, D.; Gutmann, B.; Kappe, C. O. An Experimental and Computational Assessment of Acid-Catalyzed Azide-Nitrile Cycloadditions. *J. Org. Chem.* **2012**, *77*, 10882−10890.
(55) Hiemenz, P. C.; Rajagopalan, R. *Principles of Colloid and Surface Chemistry, Revised and Expanded*; CRC Press, 2016.
(56) Cao, G. *Nanostructures and Nanomaterials: Synthesis, Properties and Applications*; World Scientific, 2004.
(57) Schneider, C. A.; Rasband, W. S.; Eliceiri, K. W. NIH Image to ImageJ: 25 Years of Image Analysis. *Nat. Methods* **2012**, *9*, 671−675.
(58) Martis, V.; Nikitenko, S.; Sen, S.; Sankar, G.; Van Beek, W.; Filinchuk, Y.; Snigireva, I.; Bras, W. Effects of X-rays on Crystal Nucleation in Lithium Disilicate. *Cryst. Growth Des.* **2011**, *11*, 2858−2865.
(59) Bras, W.; Clark, S. M.; Greaves, G. N.; Kunz, M.; Van Beek, W.; Radmilovic, V. Nanocrystal Growth in Cordierite Glass Ceramics Studied with X-ray Scattering. *Cryst. Growth Des.* **2009**, *9*, 1297−1305.
(60) Werner, P. E.; Eriksson, L.; Westdahl, M. TREOR, a Semi-Exhaustive Trial-and-Error Powder Indexing Program for All Symmetries. *J. Appl. Crystallogr.* **1985**, *18*, 367−370.
(61) Boultif, A.; Louër, D. Powder Pattern Indexing with the Dichotomy Method. *J. Appl. Crystallogr.* **2004**, *37*, 724−731.
(62) Kaminsky, W. WinXMorph: A Computer Program to Draw Crystal Morphology, Growth Sectors and Cross Sections with Export Files in VRML V2.0 Utf8-Virtual Reality Format. *J. Appl. Crystallogr.* **2005**, *38*, 566−567.
(63) Kaminsky, W. From CIF to Virtual Morphology Using the WinXMorph Program. *J. Appl. Crystallogr.* **2007**, *40*, 382−385.

https://doi.org/10.1021/acsomega.1c01272
ACS Omega XXXX, XXX, XXX−XXX